MDPI

Article

A Novel Synthesizing Strategy of 3D CoSe$_2$ Porous Hollow Flowers for High Performance Lithium–Sulfur Batteries

Wei Xu [1], Qikai Wu [1], Zhongmei Che [2], Bin Fan [1,3], Dengke Zhao [1], Shuai Wang [2,*], Aixia Han [4] and Ligui Li [1,3,*]

1 Guangzhou Key Laboratory for Surface Chemistry of Energy Materials, New Energy Research Institute, School of Environment and Energy, South China University of Technology, Guangzhou 510006, China; esweixu@mail.scut.edu.cn (W.X.); 201921045531@mail.scut.edu.cn (Q.W.); 201821035524@mail.scut.edu.cn (B.F.); 201810105181@mail.scut.edu.cn (D.Z.)

2 Shandong Provincial Key Laboratory of Molecular Engineering, School of Chemistry and Chemical Engineering, Qilu University of Technology (Shandong Academy of Sciences), Jinan 250353, China; cheche1997mm@163.com

3 Guangdong Provincial Key Laboratory of Advance Energy Storage Materials, South China University of Technology, Guangzhou 510640, China

4 Chemical Engineering College, Qinghai University, Xining 810016, China; hanaixia@tsinghua.org.cn

* Correspondence: qlwangshuai@qlu.edu.cn (S.W.); esguili@scut.edu.cn (L.L.)

Abstract: Redox kinetics of lithium polysulfides (LiPSs) conversion and poor electrical conductivity of sulfur during the charge-discharge process greatly inhibit the commercialization of high-performance lithium–sulfur (Li–S) batteries. Herein, we synthesized CoSe$_2$ porous hollow flowers (CoSe$_2$-PHF) by etching and further selenizing layered double hydroxide, which combined the high catalytic activity of transition metal compound and high electrical conductivity of selenium. The obtained CoSe$_2$-PHF can efficiently accelerate the catalytic conversion of LiPSs, expedite the electron transport, and improve utilization of active sulfur during the charge-discharge process. As a result, with CoSe$_2$-PHF/S-based cathodes, the Li–S batteries exhibited a reversible specific capacity of 955.8 mAh g^{-1} at 0.1 C and 766.0 mAh g^{-1} at 0.5 C, along with a relatively small capacity decay rate of 0.070% per cycle within 400 cycles at 1 C. Even at the high rate of 3 C, the specific capacity of 542.9 mAh g^{-1} can be maintained. This work enriches the way to prepare porous composites with high catalytic activity and electrical conductivity as sulfur hosts for high-rate, long-cycle rechargeable Li–S batteries.

Keywords: transition metal selenide; catalysis; electrical conductivity; lithium sulfur batteries

1. Introduction

Lithium-sulfur (Li–S) batteries are promising and have been intensively studied in recent years. It gains popularity due to the following reasons: (1) Li–S batteries possess high theoretical specific capacity (1675 mAh g^{-1}) and energy density (2600 kW kg^{-1}), which are desired by advanced energy storage systems such as electric vehicles; (2) The element sulfur is abundant; (3) Li–S batteries are environmentally friendly and cost-effective [1–4]. However, sluggish redox kinetics and shutting effects of LiPSs, poor electrical conductivity of sulfur (5 × 10^{-30} S/cm at 25 °C) [5,6], and severe volume expansion (up to 80%) restrict the commercialization of Li–S batteries [7–12].

Tremendous efforts have been invested in addressing the challenges mentioned above by developing novel strategies to fabricate state-of-the-art cathodes for Li–S batteries. Porous carbon materials such as mesoporous carbon, carbon nanotubes and graphene have been widely used to enhance the conductivity and mitigate the volume expansion of electrodes [13–18]. However, it is difficult to inhibit the dissolving of LiPSs into electrolyte due to the poor polarity of these carbon materials [19–22]. Research shows that a judicious method is to absorb LiPSs through chemical reactions [23]. Therefore, metallic compounds, such as metallic oxide, carbide, nitride, and sulfide have become a hotspot study in the past

several years [24–28]. Among these, transition metal oxides and sulfides exhibit superior electrochemical performance, which can promote the catalytic conversion of LiPSs [29–33]. The visualized adsorption test of polysulfides shows that titanium, vanadium and cobalt based oxides or sulfides have notable advantages of absorbing LiPSs. However, the poor conductivity of transition metal oxides and sulfides compromise their advantages of the superior cycle and rate performance for Li–S batteries.

Recently, transition metal selenides gain their popularity as potential candidates for cathode materials of high-performance Li–S batteries. It is because selenium, as the chalcogen, shares relatively similar electronegativity and ionic radius with sulfur, while has higher electrical conductivity (1×10^{-3} S/cm) [34,35]. Hence, we combined the high catalytic activity of transition metal compound and high electrical conductivity of selenium to fabricate the $CoSe_2$-PHF through etching and further selenizing layered double hydroxide. The etching process created many pores and exposed abundant active sites that could efficiently accelerate the catalytic conversion of LiPSs. The further selenizing process enhanced the electrical conductivity and improved the utilization of the active sulfur. Thanks to these merits, the batteries assembled with $CoSe_2$-PHF/S-based cathodes exhibited a reversible specific capacity of 959.2 mAh g^{-1} at 0.1 C and 766.0 mAh g^{-1} at 0.5 C, along with a relatively small capacity decay rate of 0.070% per cycle within 400 cycles at 1 C. Even at the high rate of 3 C, the specific capacity of 542.9 mAh g^{-1} can still be maintained.

2. Results and Discussion

Figure 1 presents the synthesis process of $CoSe_2$-PHF. Firstly, CoAl-LDH precursors were synthesized by the facile water bath method (The details can be seen in the experimental section). Secondly, Co-PHF were obtained by treating CoAl-LDH with 5mol L^{-1} NaOH aqueous solution for 4 h. Notably, Al^{3+} can be etched by excess NaOH in this process so that generating many pores and exposing abundant active sites of catalyzing the conversion of LiPSs. Finally, Co-PHF were mixed with selenium powder, and then were heated at 500 °C for 3 h under N_2 atmosphere to obtain $CoSe_2$-PHF.
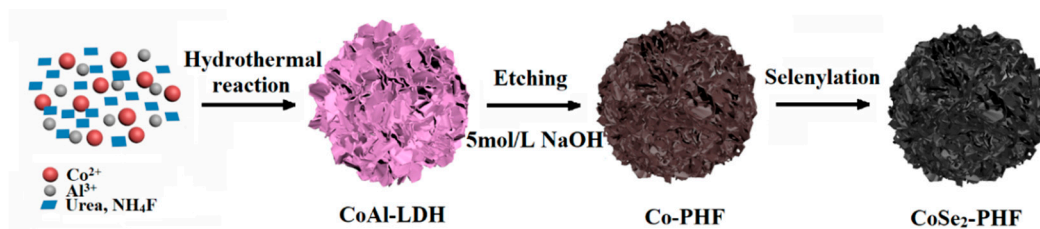

Figure 1. Schematic of synthesis process for $CoSe_2$-PHF.

As shown in Figure 2a, Co-PHF exhibited flower-like sphere with a diameter of around 10 μm. Additionally, Figure 2b clearly showed the hollow structure of Co-PHF, which would provide a large space to accommodate the volume fluctuation of active sulfur in cathodes during the cycling process. After selenylation, the obtained $CoSe_2$-PHF (Figure 2c) maintained the flower-like morphology of Co-PHF parent. The transmission electron microscope (TEM) image (Figure 2d) showed that $CoSe_2$-PHF were composed of hexagonal sheets, and the insert figure exhibited that $CoSe_2$-PHF were porous, which can expose abundant active sites towards catalyzing the conversion of LiPSs. Figure 2e showed the high-resolution TEM image of $CoSe_2$-PHF, the d-spacing lattice of $CoSe_2$-PHF was 0.237 nm, corresponding to the (211) plane of $CoSe_2$. As illustrated in Figure 2f, the SAED pattern can be well indexed according to the crystallographic data, indicating the high crystallinity of $CoSe_2$-PHF. The element distribution of $CoSe_2$-PHF, as shown in Figure 2g, indicated that Co, Se, and C were evenly distributed on the flower-like sphere, further suggesting the successful preparation of $CoSe_2$-PHF.
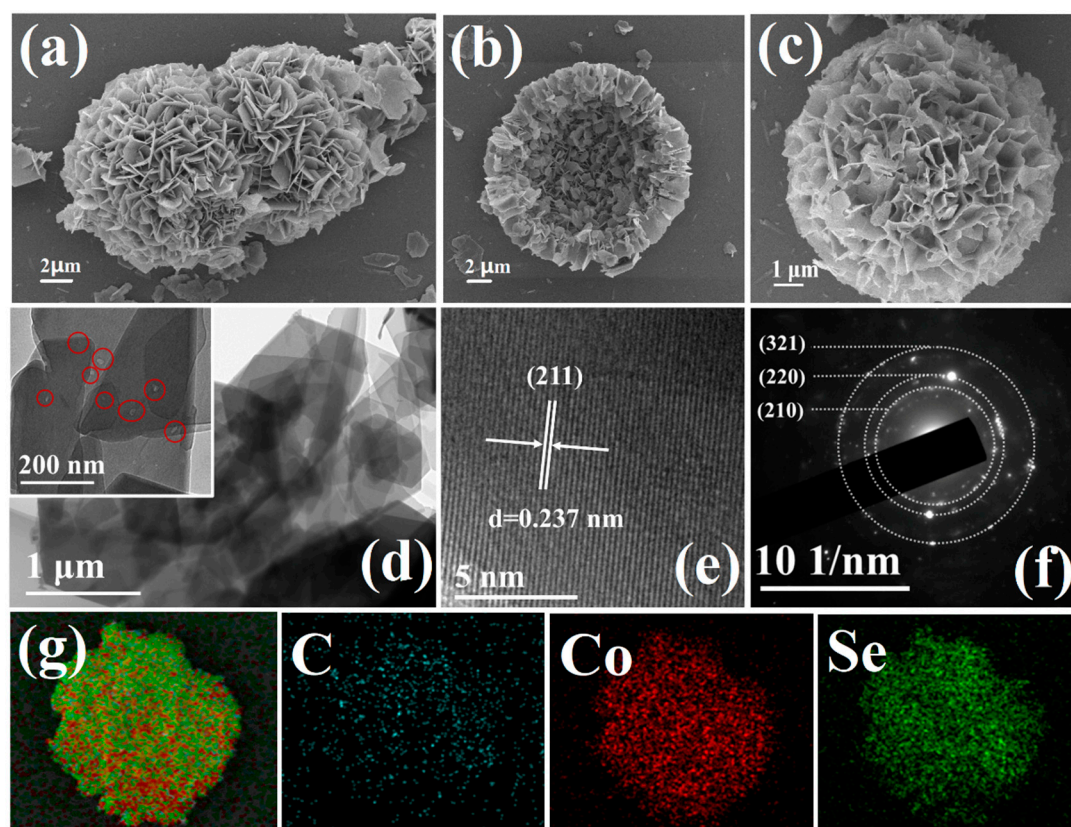
Figure 2. (**a**,**b**) SEM of Co-PHF. (**c**) SEM of CoSe$_2$-PHF, and (**d**) TEM of CoSe$_2$-PHF. (**e**) HR-TEM images of CoSe$_2$-PHF. (**f**) SAED pattern of CoSe$_2$-PHF. (**g**) Element mapping images for C, Co, and Se elements in CoSe$_2$-PHF.

Thermogravimetric analysis (TGA) was conducted to determine the sulfur loading in CoSe$_2$-PHF/S. As shown in Figure 3a, the sulfur loading in CoSe$_2$-PHF/S composite was about 74 wt%. This high sulfur loading can be ascribed to the hollow structure of CoSe$_2$-PHF. The specific surface area and pore structure of CoAl-LDH, Co-PHF and CoSe$_2$-PHF were determined by using N$_2$ adsorption/desorption measurement. All of the three samples showed the type-IV curves (Figure 3b), which implied the mesoporous structure of these samples. The BET test results for different samples were summarized in Table 1. The specific surface area of Co-PHF was measured as 40.177 m$^2 \cdot$g^{-1}, which was approximately twice to that of CoAl-LDH (19.515 m$^2 \cdot$g^{-1}). This result may be caused by the etching of NaOH in CoAl-LDH leading to the formation of porous structure in Co-PHF. After selenizing treatment, the specific surface area was decreased to 31.986 m$^2 \cdot$g^{-1} due to the formation of CoSe$_2$-PHF. These three samples' results of N$_2$ adsorption−desorption measurements were in line with their morphological features observed by SEM and TEM measurements. Figure 3c demonstrated the pore size distribution plots of the three samples tested by the Barrett−Joyner−Halenda (BJH) method. The average pore diameter of CoAl-LDH was 5.012 nm, and this value was increased to 17.296 nm after etching, and the average pore diameter was decreased to 15.310 nm with the selenizing treatment. The large specific surface and the abundant mesoporous textures of CoSe$_2$-PHF are ideal for enhancing the performance of sulfur cathodes. It is because they can provide sufficient adsorptive and catalytic sites for LiPSs, and efficiently mitigate the volume changes of the cathodes during the charge-discharge process.
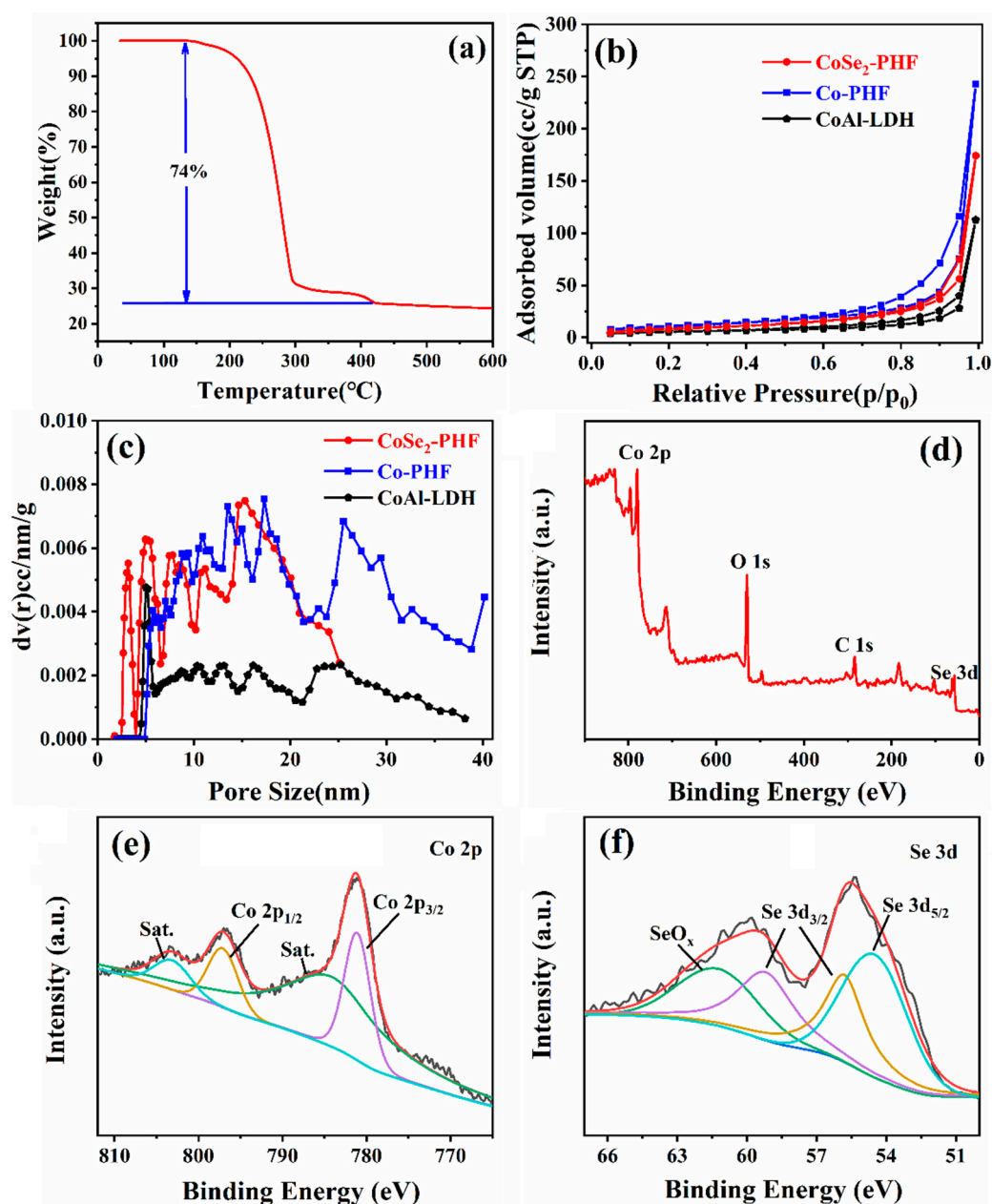
Figure 3. (**a**) TGA curve of CoSe$_2$-PHF/S, (**b**) N$_2$ adsorption and desorption isotherms, (**c**) The pore-size distribution plots, (**d**) The XPS survey spectra of CoSe$_2$-PHF, (**e**) Co 2p XPS spectra for CoSe$_2$-PHF, and (**f**) Se 3d XPS spectra for CoSe$_2$-PHF.

Table 1. Specific surface area, total pore volume and average pore diameter of different samples.

Samples	S$_{BET}$ (m$^2 \cdot$g^{-1})	Total Pore Volume (cm$^3 \cdot$g^{-1})	Mean Pore Diameter (nm)
CoAl-LDH	19.515	0.058	5.012
Co-PHF	40.177	0.169	17.296
CoSe$_2$-PHF	31.986	0.108	15.310
CoSe$_2$	18.884	0.063	8.690
CoS$_2$	19.659	0.065	9.114
Co$_3$O$_4$	22.665	0.059	8.796

X-ray photoelectron spectroscopy (XPS) tests were then conducted to explore the chemical composition and valence states of CoSe$_2$-PHF. As observed from the survey spectrum of CoSe$_2$-PHF (Figure 3d), the element of Co, Se, C and O were all existed.

According to the literature, O 1s can be ascribed to the unavoidable surface adsorption of the sample due to the exposure to the air. [36]. Peak fitting analysis of Co in 2p region showed Co $2p_{1/2}$ (797.1 eV), Co $2p_{3/2}$ (781.1 eV) and two satellite peaks (Figure 3e), which were consistent with Co^{2+} in $CoSe_2$ [36,37]. In addition, two obvious satellites at the higher energy side of the Co 2p indicated the antibonding orbital between the atom of Co and Se [38]. In Figure 3f, the peaks located at 54.5 eV and 55.8 eV were attributed to Co–Se bond, while the peak located at around 61.2 eV was assigned to SeO_x, which was formed by partial oxidation of $CoSe_2$ [36,37,39,40].

Figure 4a,b displayed the x-ray diffraction (XRD) patterns of Co-PHF, $CoSe_2$-PHF, and $CoSe_2$-PHF/S. Although most of the aluminum in the precursor (CoAl-LDH) was etched by NaOH, the diffraction peaks of Co-PHF were still matched well with CoAl-LDH (PDF#51-0045) [41–43]. After selenylation, since that the characteristic diffraction peaks of $CoSe_2$ (PDF#09-0234) appear in the obtained $CoSe_2$-PHF sample. In addition, the XRD pattern of $CoSe_2$-PHF/S composite is actually the overlap of XRD peaks of $CoSe_2$-PHF and S_8, indicating that sulfur is successfully loaded into $CoSe_2$-PHF.
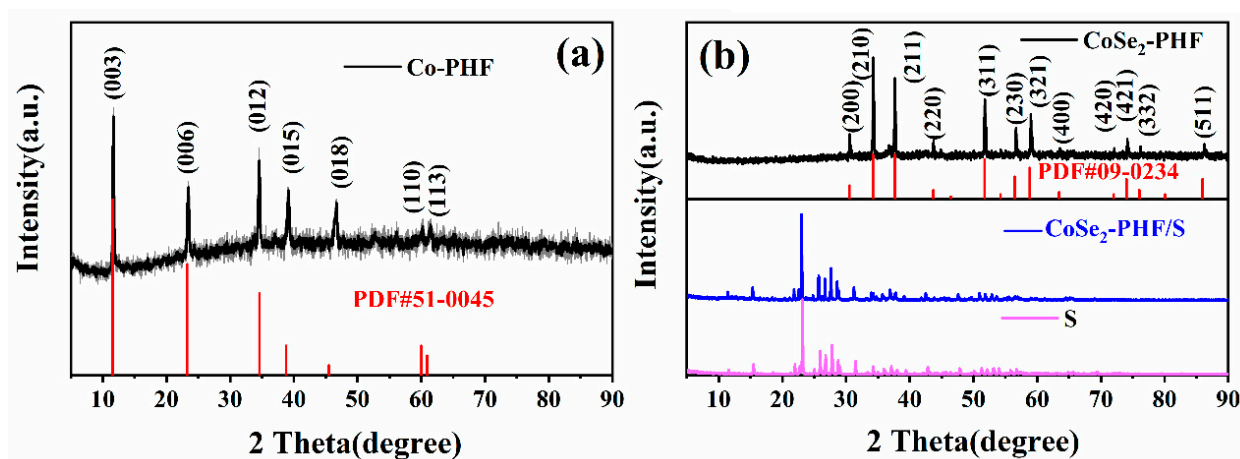

Figure 4. XRD patterns of (**a**) Co-PHF, and (**b**) $CoSe_2$-PHF & $CoSe_2$-PHF/S.

Cyclic voltammetry (CV) was conducted to investigate the catalytic activity of $CoSe_2$-PHF toward the conversion of LiPSs in the charge-discharge process. As shown in Figure 5a, two reduction peaks (R_1 and R_2) and one oxidation peak (O) were observed in both $CoSe_2$-PHF/S and $CoSe_2$/S electrodes. For $CoSe_2$/S-based electrode, the first reduction peak (R_1) corresponded to the conversion of sulfur (S_8) to long-chain Li_2S_n ($4 \leq n \leq 8$), and the second reduction peak (R_2) was related to the further reduction of long-chain LiPSs to short-chain Li_2S_2 and LiS_2, as well as $CoSe_2$-PHF/S based electrode [44–46]. The broad oxidation peak centered at about 2.455 V represented the two continuous oxidation processes. As shown in Figure 5b and Figure S2 (see Supplementary Materials), both reduction and oxidation peaks were highly dependent on the potential scan rate. As the potential scan rate increased, two reduction peaks shifted to lower potential while the oxidation peak shifted to higher potential. Significantly, the area ratio of reduction peak to oxidation peak for $CoSe_2$-PHF/S electrode was close to 1, indicating its highly reversible reaction of sulfur redox. By contrast, the two reduction peaks of $CoSe_2$/S-based electrode centered at lower potential (2.238 V, and 2.027 V, respectively), and the oxidation peak centered at a higher potential (2.487 V), which suggested that $CoSe_2$-PHF possessed higher catalytic activity than $CoSe_2$. And CV tests on the symmetrical cells of $CoSe_2$-PHF electrode and $CoSe_2$ electrode (without loading sulfur) showed the same conclusion. As shown in Figure 5c, the redox current in $CoSe_2$-PHF cell increased faster than that of $CoSe_2$-based cell with the increasing of potential, implying that $CoSe_2$-PHF electrode can really accelerate the conversion of LiPSs and enhance the kinetics of electrode reaction.
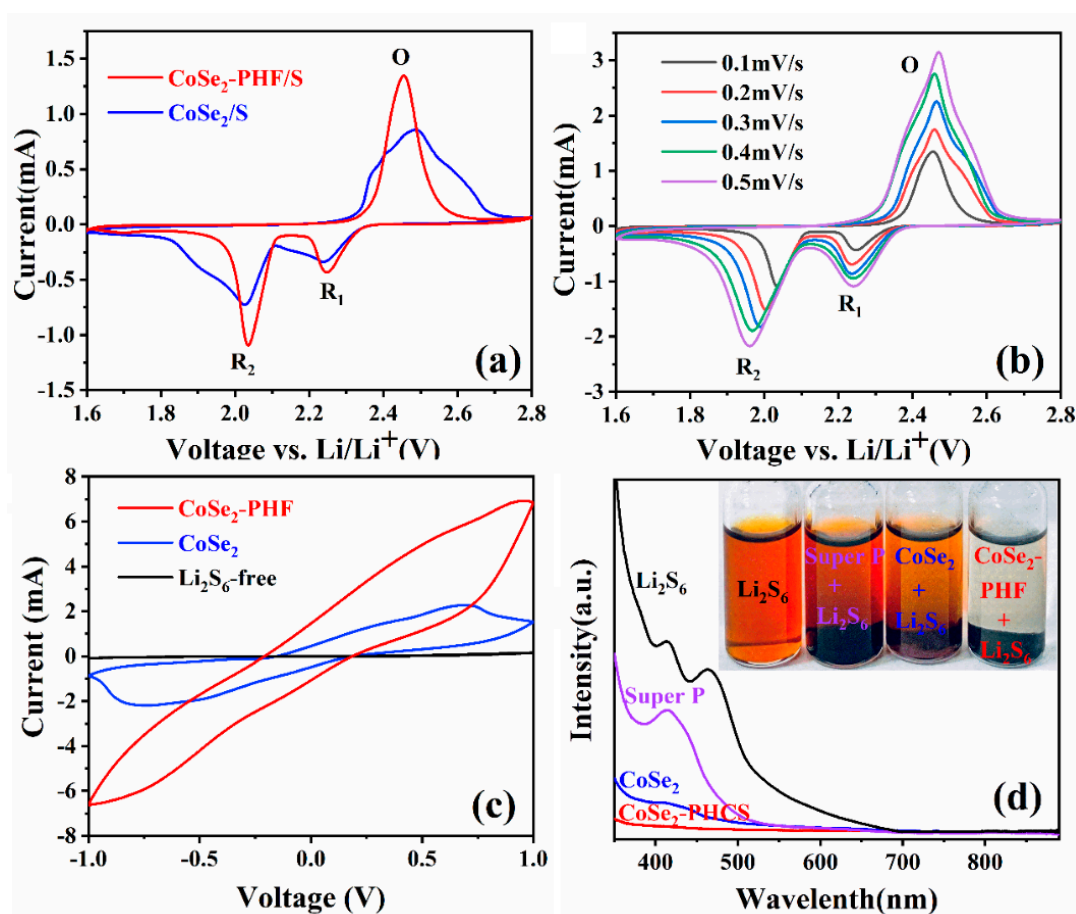
Figure 5. (**a**) CV curves of CoSe$_2$-PHF/S and CoSe$_2$/S cathodes at a scan rate of 0.1 mV s^{-1}, (**b**) CV curves of CoSe$_2$-PHF/S under different scan rates, (**c**) CV profiles for symmetric cells, (**d**) Photograph and UV−vis absorption spectra of polysulfides solutions with the addition of Super P, CoSe$_2$, and CoSe$_2$-PHF.

Theoretically, CoSe$_2$-PHF could inhibit the shuttle effect of polysulfides via the enhanced chemical absorption and catalytic conversion between CoSe$_2$-PHF and LiPSs. As shown in Figure 5d, LiPSs solution (Li$_2$S$_6$, 0.5 mol·L^{-1}) was soaked with the CoSe$_2$-PHF for 2 h and its color was changed from brown to almost water white, while the other two solutions (added with Super P, and CoSe$_2$, respectively) were changed slightly, which corresponded with the results of UV−vis absorption spectra, indicating the much stronger adsorption and catalytic conversion capability for LiPSs of CoSe$_2$-PHF.

Electrical conductivity measurements revealed the conductivity of CoSe$_2$-PHF. As shown in Table 2, the electrical conductivity for CoSe$_2$-PHF was estimated to be 1.49 × 10^{-2} S cm^{-1}, which is an increase of nearly 3 orders of magnitude compared with Co$_3$O$_4$ (1.90 × 10^{-5} S cm^{-1}) and CoS$_2$ (2.27 × 10^{-5} S cm^{-1}). The high electrical conductivity of CoSe$_2$-PHF is beneficial for the electron transport and utilization of active sulfur during the charge-discharge process. Furthermore, electrochemical impedance spectra (EIS) of CoSe$_2$-PHF/S cathodes before charge-discharge process were conducted to determine the internal resistance and charge transfer kinetics (Co$_3$O$_4$/S, CoS$_2$/S and CoSe$_2$/S cathodes as contrast samples). As shown in Figure 6, the Nyquist plots of CoSe$_2$-PHF/S and other three contrast electrodes showed semicircles in the high frequency region (charge-transfer resistance, R$_{ct}$) [35,47]. The R$_{ct}$ of electrode−electrolyte interface for CoSe$_2$-PHF/S, CoSe$_2$/S, CoS$_2$/S and Co$_3$O$_4$/S cathodes was 38.509 Ω, 55.526 Ω, 74.221 Ω, and 84.337 Ω, respectively, indicating the lower resistance for charge transfer and faster kinetics for LiPSs conversion in CoSe$_2$-PHF/S [48]. Therefore, CoSe$_2$-PHF can significantly reduce charge-transfer resistance and promote the electrode reaction kinetics of LiPSs.

Table 2. Electrical conductivity of different samples.

Samples	σ (S cm^{-1})
S [5]	5.00×10^{-30}
Co_3O_4	2.27×10^{-5}
CoS_2	1.90×10^{-5}
$CoSe_2$	2.57×10^{-3}
$CoSe_2$-PHF	1.49×10^{-2}
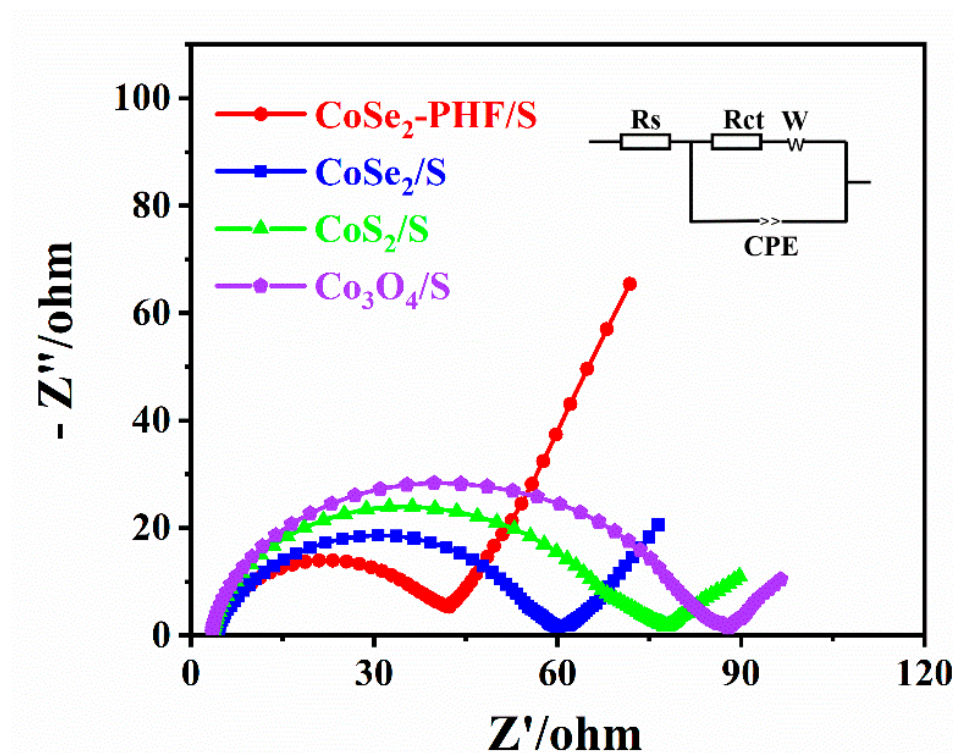
Figure 6. Electrochemical impedance spectra of $CoSe_2$-PHF/S, $CoSe_2$/S, CoS_2/S, and Co_3O_4/S cathodes.

To further study the electrochemical performance of $CoSe_2$-PHF/S electrodes, a series of charge-discharge cycling experiments were tested. As shown in Figure 7a,b, $CoSe_2$-PHF/S electrodes showed much higher discharge capacity than $CoSe_2$/S electrodes at any discharge voltage. In Figure 7c, the ratio of Q2 (Corresponding to Li_2S_4 + 2e$^-$ + 2Li$^+$ → 2Li$_2$S$_2$; Li_2S_2 + 2e$^-$ + 2Li$^+$ → 2Li$_2$S) to Q1 (Corresponding to S$_8$ + 4e$^-$ + 4Li$^+$ → 2Li$_2$S$_4$) for $CoSe_2$-PHF/S and $CoSe_2$/S electrodes were 2.64, and 1.63, respectively. The charge-discharge voltage gap (ΔE) of $CoSe_2$-PHF/S electrodes were much smaller than that of $CoSe_2$/S (Figure 7c,d) [49–51], suggesting the faster ions transport and lower electrochemical polarization of $CoSe_2$-PHF/S electrodes.

The corresponding voltage profiles based on different current rates were shown in Figure 8a. The discharge platform at a relatively high current rate of 3 C maintained well in $CoSe_2$-PHF/S electrodes, suggesting a high operation stability of $CoSe_2$-PHF/S electrodes. The value of rate capacity for $CoSe_2$-PHF/S electrodes were 955.8 mAh g^{-1} at 0.1 C, 769.6 mAh g^{-1} at 0.5 C, 680.7 mAh g^{-1} at 1 C, 618.0 mAh g^{-1} at 2 C, and 542.9 mAh g^{-1} at 3 C (Figure 8b), which were much higher than these of $CoSe_2$/S, CoS_2/S and Co_3O_4/S. At the current rate of 0.1 C, $CoSe_2$-PHF/S electrodes with sulfur loading at 1.3 mg cm^{-2} showed a much higher specific capacity other electrodes in each cycle (Figure 8c). Besides, with a high sulfur loading at 3.4 mg cm^{-2} (Figure 8d), initial specific capacity of $CoSe_2$-PHF/S electrodes were 578.8 mAh g^{-1}, which could retain 86.3% of its initial capacity after 150 cycles at 0.5 C. The decrease of specific capacity with the increasing of sulfur loading may be caused by the quick dissolution of LiPSs intermediates

into electrolyte. To further verify the electrochemical performance of CoSe$_2$-PHF/S electrodes, long-term cycling was also conducted at 1 C. As shown in Figure 8e, in contrast to CoSe$_2$/S, CoSe$_2$/S, CoS$_2$/S and Co$_3$O$_4$/S electrodes, which displayed much lower specific capacities and coulombic efficiencies, CoSe$_2$-PHF/S electrodes can retain a high capacity of 522.1 mAh g^{-1} and a nearly 100% coulombic efficiency after 400 cycles, corresponding to a slow capacity decay rate of 0.070% per cycle. Therefore, CoSe$_2$-PHF/S electrodes owned much better electrochemical performance, and can be considered as a promising sulfur host for Li$-$S batteries.
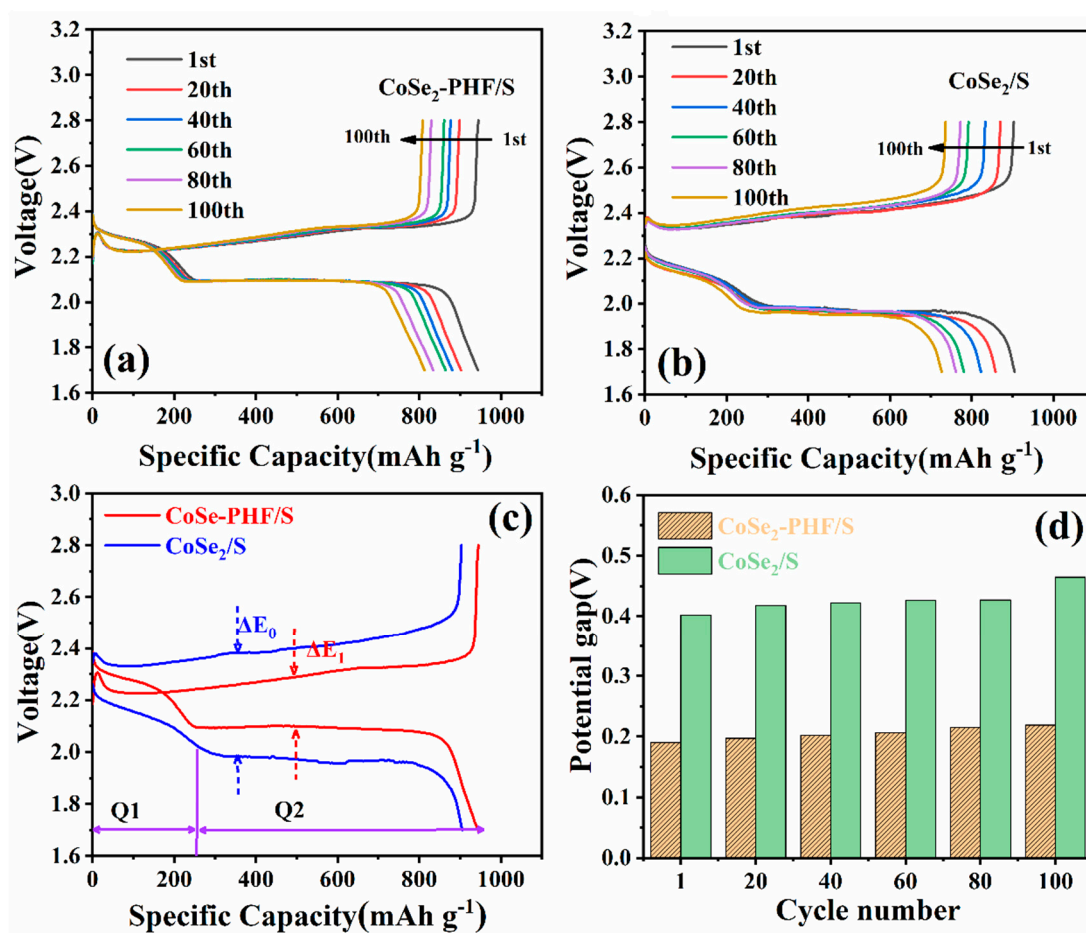

Figure 7. Charge$-$discharge cycling curves of (**a**) CoSe$_2$-PHF/S based and (**b**) CoSe$_2$/S based electrodes at a 0.1 C, (**c**) Galvanostatic discharge$-$charge voltage profiles of the first cycle at 0.1 C, (**d**) potential gap of CoSe$_2$-PHF/S and CoSe$_2$/S based electrodes at various charge$-$discharge cycles.

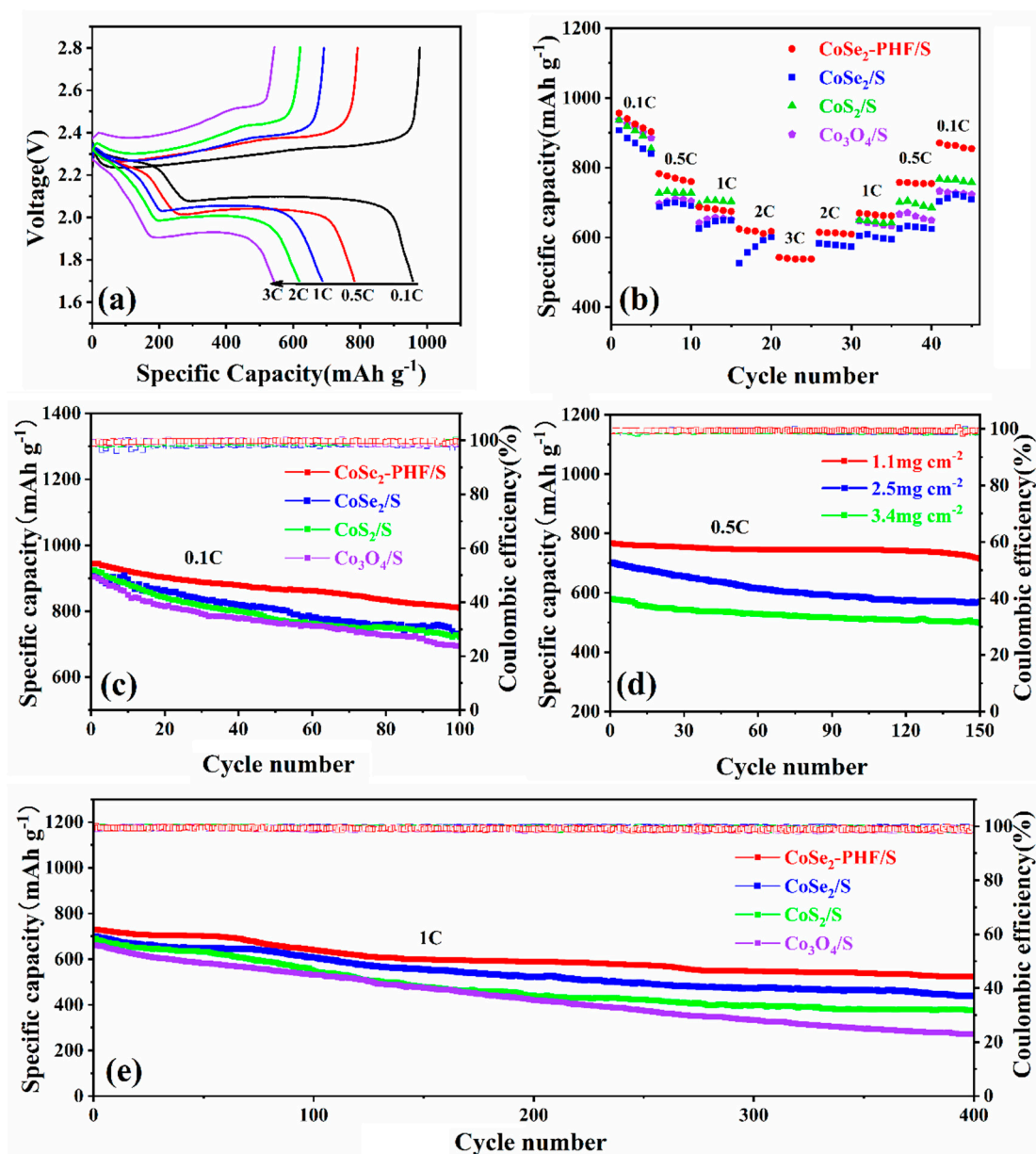**Figure 8.** (**a**) Galvanostatic charge−discharge curves for $CoSe_2$-PHF/S based electrodes at different current rates, (**b**) Rate performance of $CoSe_2$-PHF/S, $CoSe_2$/S, CoS_2/S, and Co_3O_4/S based electrodes at various current rates, (**c**) Cycling performance of $CoSe_2$-PHF/S, $CoSe_2$/S, CoS_2/S, and Co_3O_4/S based electrodes at 0.1 C with the sulfur loading of 1.3 mg cm^{-1}, (**d**) Specific capacity of $CoSe_2$-PHF/S with varied sulfur loadings at 0.5 C, (**e**) Cycling performance of $CoSe_2$-PHF/S, $CoSe_2$/S, CoS_2/S, and Co_3O_4/S based electrodes at 1 C with the sulfur loading of 1.2 mg cm^{-2}.

3. Experimental Section

3.1. Synthesis of CoAl-LDH Precursors

CoAl-LDH precursors were prepared by a typical hydrothermal process. Firstly, Co $(NO_3)_2$ $6H_2O$ (2.183 g), Al $(NO_3)_3$ $9H_2O$ (0.938 g), NH_4F (0.371 g) and urea (1.501 g) were dissolved in 50 mL deionized water (DIW) and stirred at room temperature for 1 h. Secondly, the solution was added into a 100 mL Teflon-lined stainless-steel autoclave and maintained at 110 °C for 8 h. After cooling to room temperature, the precipitates were obtained by centrifuging and washing with DIW for several times. Finally, CoAl-LDH precursors were obtained by drying at 60 °C for 12 h.

3.2. Synthesis of CoSe₂-PHF, CoSe₂, CoS₂ and Co₃O₄

3.2. Synthesis of CoSe$_2$-PHF, CoSe$_2$, CoS$_2$ and Co$_3$O$_4$

Firstly, 20 g of NaOH and 1 g CoAl-LDH precursors were dispersed in 200 mL DIW and stirred for 4 h. Secondly, the brown precipitates (denoted as Co-PHF) were collected by centrifuging and washing with DIW for several times, followed by drying at 60 °C overnight. Finally, 200 mg of Co-PHF were mixed with 800 mg of selenium powder, and then the mixture was heated at 500 °C for 3 h under N_2 atmosphere to obtain $CoSe_2$-PHF. For comparison, Co_3O_4 was prepared by heating Co-PHF in the air at 500 °C for 3 h; CoS_2 was prepared by heating the mixture of Co-PHF and sulfur at 500 °C for 3 h under N_2 atmosphere, and $CoSe_2$ was prepared by heating the mixture of CoAl-LDH precursors and selenium powder at 500 °C for 3 h under N_2 atmosphere.

3.3. Synthesis of CoSe$_2$-PHF/S, CoS$_2$/S and Co$_3$O$_4$/S and CoSe$_2$/S Composite

Sulfur was thoroughly mixed with $CoSe_2$-PHF at a mass ratio of 3:1. Subsequently, the mixture was heated under Ar atmosphere at 155 °C for 12 h and then further treated at 200 °C for 1 h in a quartz tubular furnace. The resultant samples were defined as $CoSe_2$-PHCS/S composite. CoS_2/S and Co_3O_4/S and $CoSe_2$/S were also prepared in the same method.

3.4. Visualized Adsorption Test of Polysulfides

Li_2S_6 (0.5 mol L^{-1}) solution was prepared by dissolving sulfur and Li_2S at a molar ratio of 5:1 in a mixture of dimethoxyethane (DME) and 1,3-dioxolane (DOL) (*v/v*, 1:1), and vigorously stirring at 65 °C in an Ar-filled glovebox. Subsequently, 20.0 mg of samples (i.e., $CoSe_2$-PHF and $CoSe_2$) were added to 5.0 mL of Li_2S_6 solution for a 2 h static adsorption to evaluate their LiPSs adsorption ability.

3.5. Electrochemical Measurement

The cathodes were prepared by mixing $CoSe_2$-PHF/S (or Co_3O_4/S, CoS_2/S, and $CoSe_2$/S) composite, Super P, and PVDF in NMP (7:2:1) and stirring the mixtures for 6 h, then coating the obtained slurry on Al foil and drying in an oven at 60 °C for 24 h. CR2016 coin cells were assembled in the glovebox and the sulfur areal mass loading of the batteries is 1.1–1.5 mg cm^{-2}. Celgard 2400 film was placed between cathode and lithium foil. The electrolyte was consisted of 1.0 M LiTFSI, a mixture of DOL and DME (1:1, *v/v*), and 2.0 wt% $LiNO_3$ additive. The cycling and rate performance were tested on the LAND battery test instrument (LAND CT2001A, Wuhan, China) between 1.6 V and 2.8 V. Cyclic voltammetry curves and electrochemical impedance spectra were obtained with the electro-chemical workstation (CHI660D, Shanghai, China).

3.6. Characterization

The morphologies of the materials were investigated by using a Hitachi SU8010 field-emission SEM (Hitachi, Tokyo, Japan). The TEM images were investigated by a JEOL JEM-2100F microscope. The crystal structures were obtained by using a Bruker D8 Advance powder X-ray diffract meter at the 2θ range of 5–90°. TGA curves were obtained with a METTLER instrument. The samples were tested under a N_2 atmosphere at a heating rate of 10 °C min^{-1}. XPS measurements were conducted with a Phi X-tool XPS instrument. BET specific surface area and porous structure were determined by a Micromeritics ASAP 2020 analyzer. Electrical conductivity was determined by using a four-point probe resistivity measurement system (RTS-9).

4. Conclusions

In conclusion, $CoSe_2$-PHF were prepared by a novel synthesizing strategy of etching and further selenizing CoAl-LDH. Due to the porous transition metal compound's superior adsorption and catalytic conversion capabilities towards LiPSs and the high electrical conductivity of metal sulfides, $CoSe_2$-PHF can not only efficiently accelerate the catalytic conversion of LiPSs during the charge-discharge process, but also expedite the electron

transport and improve the utilization of the active sulfur. As a result, $CoSe_2$-PHF/S cathode materials in Li−S batteries exhibit a reversible specific capacity of 955.8 mAh g^{-1} at 0.1 C and 766.0 mAh g^{-1} at 0.5 C, along with a small capacity decay rate of 0.070% per cycle within 400 cycles at 1 C. Even at the high rate of 3 C, the specific capacity of 542.9 mAh g^{-1} can be maintained. This work offers a new way to prepare porous composites with high catalytic activity and electrical conductivity as efficient sulfur hosts for high-rate, long-cycle rechargeable Li−S batteries.

Supplementary Materials: The following are available online at https://www.mdpi.com/2073-4344/11/2/273/s1, Figure S1: (a) XRD of $CoSe_2$, (b) XRD of CoS_2, (c) XRD of Co_3O_4, Figure S2: CV curves of $CoSe_2$ under different scan rates.

Author Contributions: W.X. conducted the experiments and wrote the paper; Q.W., B.F. and D.Z. conducted part of the experiments; Z.C., A.H., S.W. and L.L. helped revise the paper and edit the figures. All authors have read and agreed to the published version of the manuscript.

Institutional Review Board Statement: Not applicable.

Informed Consent Statement: Not applicable.

Data Availability Statement: The data presented in this study are available on request from the corresponding author.

Conflicts of Interest: The authors declare no conflict of interest.

References

1. Chen, L.; Yang, W.; Liu, J.; Zhou, Y. Decorating $CoSe_2$ hollow nanospheres on reduced graphene oxide as advanced sulfur host material for performance enhanced lithium-sulfur batteries. *Nano Res.* **2019**, *12*, 2743–2748.
2. Rana, M.; Ahad, S.A.; Li, M.; Luo, B.; Wang, L.; Gentle, I.; Knibbe, R. Review on areal capacities and long-term cycling performances of lithium sulfur battery at high sulfur loading. *Energy Storage Mater.* **2019**, *18*, 289–310.
3. Yu, J.; Khan, S.A.; Zhao, D.; Li, L.; Wu, Z.; Niu, X.; Chen, S. Nitrogen and iron codoped porous carbon polyhedra for effectively confining polysulfides and efficiently catalyzing their conversion in lithium–sulfur batteries. *Sustain. Energy Fuels* **2020**, *4*, 5215–5222.
4. Zhao, J.; Zhao, D.; Li, L.; Zhou, L.; Liang, X.; Wu, Z.; Jiang, Z.-J. Defect-rich, mesoporous cobalt sulfide hexagonal nanosheets as superior sulfur hosts for high-rate, long-cycle rechargeable lithium–sulfur batteries. *J. Phys. Chem. C* **2020**, *124*, 12259–12268.
5. Zeng, S.; Li, L.; Yu, J.; Wang, N.; Chen, S. Highly crosslinked organosulfur copolymer nanosheets with abundant mesopores as cathode materials for efficient lithium-sulfur batteries. *Electrochim. Acta* **2018**, *263*, 53–59.
6. Tsao, Y.; Lee, M.; Miller, E.C.; Gao, G.; Park, J.; Chen, S.; Katsumata, T.; Tran, H.; Wang, L.-W.; Toney, M.F.; et al. Designing a quinone-based redox mediator to facilitate Li_2S oxidation in Li–S batteries. *Joule* **2019**, *3*, 872–884.
7. Li, T.; Bai, X.; Gulzar, U.; Bai, Y.J.; Capiglia, C.; Deng, W.; Zhou, X.; Liu, Z.; Feng, Z.; Proietti Zaccaria, R. A comprehensive understanding of lithium–sulfur battery technology. *Adv. Funct. Mater.* **2019**, *29*, 1901730.
8. Wang, X.L.; Chen, J.; Jin, B.; Jiang, Q.; Jin, E.M.; Jeong, S.M. Electrochemical performance of electrospun lotus-root-structure porous multichannel carbon nanotubes for lithium–sulfur battery applications. *J. Electroanal. Chem.* **2020**, *878*, 114564.
9. Xu, N.; Qian, T.; Liu, X.; Liu, J.; Chen, Y.; Yan, C. Greatly suppressed shuttle effect for improved lithium sulfur battery performance through short chain intermediates. *Nano Lett.* **2017**, *17*, 538–543.
10. Xie, J.; Li, B.Q.; Peng, H.J.; Song, Y.W.; Zhao, M.; Chen, X.; Zhang, Q.; Huang, J.Q. Implanting atomic cobalt within mesoporous carbon toward highly stable lithium–sulfur batteries. *Adv. Mater.* **2019**, *31*, 1903813.
11. Zhao, M.; Li, B.Q.; Zhang, X.Q.; Huang, J.Q.; Zhang, Q. A perspective toward practical lithium–sulfur batteries. *ACS Cent. Sci.* **2020**, *6*, 1095–1104.
12. Shaibani, M.; Sharifzadeh Mirshekarloo, M.; Singh, R.; Easton, C.D.; Cooray, M.C.D.; Eshraghi, N.; Abendroth, T.; Dörfler, S.; Althues, H.; Kaskel, S.; et al. Expansion-tolerant architectures for stable cycling of ultrahigh-loading sulfur cathodes in lithium-sulfur batteries. *Sci. Adv.* **2020**, *6*, eaay2757. [CrossRef]

13. Gueon, D.; Hwang, J.T.; Yang, S.B.; Cho, E.; Sohn, K.; Yang, D.K.; Moon, J.H. Spherical macroporous carbon nanotube particles with ultrahigh sulfur loading for lithium-sulfur battery cathodes. *ACS Nano* **2018**, *12*, 226–233.

14. Jayaprakash, N.; Shen, J.; Moganty, S.S.; Corona, A.; Archer, L.A. Porous hollow carbon@sulfur composites for high-power lithium-sulfur batteries. *Angew. Chem. Int. Ed. Engl.* **2011**, *50*, 5904–5908.

15. Li, M.; Carter, R.; Douglas, A.; Oakes, L.; Pint, C.L. Sulfur vapor-infiltrated 3D carbon nanotube foam for binder-free high areal capacity lithium-sulfur battery composite cathodes. *ACS Nano* **2017**, *11*, 4877–4884.

16. Li, S.; Jin, B.; Zhai, X.; Li, H.; Jiang, Q. Review of carbon materials for lithium-sulfur batteries. *ChemistrySelect* **2018**, *3*, 2245–2260.

17. Song, J.; Gordin, M.L.; Xu, T.; Chen, S.; Yu, Z.; Sohn, H.; Lu, J.; Ren, Y.; Duan, Y.; Wang, D. Strong lithium polysulfide chemisorption on electroactive sites of nitrogen-doped carbon composites for high-performance lithium-sulfur battery cathodes. *Angew. Chem. Int. Ed. Engl.* **2015**, *54*, 4325–4329.

18. Zhang, Z.; Kong, L.-L.; Liu, S.; Li, G.-R.; Gao, X.-P. A high-efficiency sulfur/carbon composite based on 3D graphene nanosheet@carbon nanotube matrix as cathode for lithium-sulfur battery. *Adv. Energy Mater.* **2017**, *7*, 1602543.

19. Zeng, S.; Li, L.; Xie, L.; Zhao, D.; Zhou, N.; Wang, N.; Chen, S. Graphene-supported highly crosslinked organosulfur nanoparticles as cathode materials for high-rate, long-life lithium-sulfur battery. *Carbon* **2017**, *122*, 106–113.

20. Zheng, C.; Niu, S.; Lv, W.; Zhou, G.; Li, J.; Fan, S.; Deng, Y.; Pan, Z.; Li, B.; Kang, F.; et al. Propelling polysulfides transformation for high-rate and long-life lithium–sulfur batteries. *Nano Energy* **2017**, *33*, 306–312.

21. Kong, L.; Li, B.-Q.; Peng, H.-J.; Zhang, R.; Xie, J.; Huang, J.-Q.; Zhang, Q. Porphyrin-derived graphene-based nanosheets enabling strong polysulfide chemisorption and rapid kinetics in lithium-sulfur batteries. *Adv. Energy Mater.* **2018**, *8*, 1800849.

22. Zhou, G.; Sun, J.; Jin, Y.; Chen, W.; Zu, C.; Zhang, R.; Qiu, Y.; Zhao, J.; Zhuo, D.; Liu, Y.; et al. Sulfiphilic nickel phosphosulfide enabled Li_2S impregnation in 3D graphene cages for Li–S batteries. *Adv. Mater.* **2017**, *29*, 1603366.

23. Fan, X.; Sun, W.; Meng, F.; Xing, A.; Liu, J. Advanced chemical strategies for lithium–sulfur batteries: A review. *Green Energy Environ.* **2018**, *3*, 2–19.

24. Jiang, G.; Xu, F.; Yang, S.; Wu, J.; Wei, B.; Wang, H. Mesoporous, conductive molybdenum nitride as efficient sulfur hosts for high-performance lithium-sulfur batteries. *J. Power Sources* **2018**, *395*, 77–84.

25. Liu, Y.T.; Han, D.D.; Wang, L.; Li, G.R.; Liu, S.; Gao, X.P. $NiCo_2O_4$ nanofibers as carbon-free sulfur immobilizer to fabricate sulfur-based composite with high volumetric capacity for lithium–sulfur battery. *Adv. Energy Mater.* **2019**, *9*, 1803477.

26. Pu, J.; Shen, Z.; Zheng, J.; Wu, W.; Zhu, C.; Zhou, Q.; Zhang, H.; Pan, F. Multifunctional Co_3S_4@sulfur nanotubes for enhanced lithium-sulfur battery performance. *Nano Energy* **2017**, *37*, 7–14.

27. Tang, X.; Guo, X.; Wu, W.; Wang, G. 2D metal carbides and nitrides (MXenes) as high-performance electrode materials for lithium-based batteries. *Adv. Energy Mater.* **2018**, *8*, 1801897.

28. Zhao, M.; Peng, H.J.; Zhang, Z.W.; Li, B.Q.; Chen, X.; Xie, J.; Chen, X.; Wei, J.Y.; Zhang, Q.; Huang, J.Q. activating inert metallic compounds for high-rate lithium-sulfur batteries through in situ etching of extrinsic metal. *Angew. Chem. Int. Ed. Engl.* **2019**, *58*, 3779–3783.

29. Chen, L.; Li, X.; Xu, Y. Recent advances of polar transition-metal sulfides host materials for advanced lithium–sulfur batteries. *Funct. Mater. Lett.* **2018**, *11*, 1840010.

30. Guo, T.; Song, Y.; Sun, Z.; Wu, Y.; Xia, Y.; Li, Y.; Sun, J.; Jiang, K.; Dou, S.; Sun, J. Bio-templated formation of defect-abundant VS_2 as a bifunctional material toward high-performance hydrogen evolution reactions and lithium−sulfur batteries. *J. Energy Chem.* **2020**, *42*, 34–42.

31. Li, Y.; Jiang, T.; Yang, H.; Lei, D.; Deng, X.; Hao, C.; Zhang, F.; Guo, J. A heterostuctured Co_3S_4/MnS nanotube array as a catalytic sulfur host for lithium–sulfur batteries. *Electrochim. Acta* **2020**, *330*, 135311.

32. Zhang, K.; Chen, F.; Pan, H.; Wang, L.; Wang, D.; Jiang, Y.; Wang, L.; Qian, Y. Study on the effect of transition metal sulfide in lithium–sulfur battery. *Inorg. Chem. Front.* **2019**, *6*, 477–481.

33. Zhou, G.; Zhao, S.; Wang, T.; Yang, S.Z.; Johannessen, B.; Chen, H.; Liu, C.; Ye, Y.; Wu, Y.; Peng, Y.; et al. Theoretical calculation guided design of single-atom catalysts toward fast kinetic and long-life Li–S batteries. *Nano Lett.* **2020**, *20*, 1252–1261.

34. Choi, S.H.; Kang, Y.C. Fullerene-like $MoSe_2$ nanoparticles-embedded CNT balls with excellent structural stability for highly reversible sodium-ion storage. *Nanoscale* **2016**, *8*, 4209–4216.

35. Zhang, C.; Biendicho, J.J.; Zhang, T.; Du, R.; Li, J.; Yang, X.; Arbiol, J.; Zhou, Y.; Morante, J.R.; Cabot, A. Combined high catalytic activity and efficient polar tubular nanostructure in urchin-like metallic $NiCo_2Se_4$ for high-performance lithium–sulfur batteries. *Adv. Funct. Mater.* **2019**, *29*, 1903842.

36. Zhu, Y.; Huang, Z.; Hu, Z.; Xi, L.; Ji, X.; Liu, Y. 3D interconnected ultrathin cobalt selenide nanosheets as cathode materials for hybrid supercapacitors. *Electrochim. Acta* **2018**, *269*, 30–37.

37. Zhang, H.; Yang, B.; Wu, X.; Li, Z.; Lei, L.; Zhang, X. Polymorphic $CoSe_2$ with mixed orthorhombic and cubic phases for highly efficient hydrogen evolution reaction. *ACS Appl. Mater. Interfaces* **2015**, *7*, 1772–1779.

38. Liu, Y.; Cheng, H.; Lyu, M.; Fan, S.; Liu, Q.; Zhang, W.; Zhi, Y.; Wang, C.; Xiao, C.; Wei, S.; et al. Low overpotential in vacancy-rich ultrathin $CoSe_2$ nanosheets for water oxidation. *J. Am. Chem. Soc.* **2014**, *136*, 15670–15675.

39. Chen, T.; Li, S.; Wen, J.; Gui, P.; Guo, Y.; Guan, C.; Liu, J.; Fang, G. Rational construction of hollow core-branch $CoSe_2$ nanoarrays for high-performance asymmetric supercapacitor and efficient oxygen evolution. *Small* **2017**, *14*, 1700979.

40. Kim, J.K.; Park, G.D.; Kim, J.H.; Park, S.K.; Kang, Y.C. Rational design and synthesis of extremely efficient macroporous $CoSe_2$-CNT composite microspheres for hydrogen evolution reaction. *Small* **2017**, *13*, 1700068.

41.　Han, S.; Chang, X.; Wu, D.; Chen, H.; Chen, D.; Liu, P.; Huang, T.; Jiang, X.; Huang, Q.; Lin, H. Hierarchically porous cobalt aluminum layered double hydroxide flowers with enhanced capacitance performances. *J. Mater. Sci.* **2017**, *52*, 6081–6092.

42.　Jing, C.; Liu, X.; Yao, H.; Yan, P.; Zhao, G.; Bai, X.; Dong, B.; Dong, F.; Li, S.; Zhang, Y. Phase and morphology evolution of CoAl-LDH nanosheets towards advanced supercapacitor applications. *CrystEngComm* **2019**, *21*, 4934–4942.

43.　Zhang, Y.; Du, D.; Li, X.; Sun, H.; Li, L.; Bai, P.; Xing, W.; Xue, Q.; Yan, Z. Electrostatic self-assembly of sandwich-like CoAl-LDH/polypyrrole/graphene nanocomposites with enhanced capacitive performance. *ACS Appl. Mater. Interfaces* **2017**, *9*, 31699–31709.

44.　Li, Y.; Wu., J; Zhang, B.; Wang, W.; Zhang, G.; Seh, Z.W.; Zhang, N.; Sun, J.; Huang, L.; Jiang, J.; et al. Fast conversion and controlled deposition of lithium (poly) sulfides in lithium-sulfur batteries using high-loading cobalt single atoms. *Energy Storage Mater.* **2020**, *30*, 250–259.

45.　Sun, Z.; Vijay, S.; Heenen, H.H.; Eng, A.Y.S.; Tu, W.; Zhao, Y.; Koh, S.W.; Gao, P.; Seh, Z.W.; Chan, K.; et al. Catalytic polysulfide conversion and physiochemical confinement for lithium–sulfur batteries. *Adv. Energy Mater.* **2020**, *10*, 1904010.

46.　Wu, X.; Liu, N.; Wang, M.; Qiu, Y.; Guan, B.; Tian, D.; Guo, Z.; Fan, L.; Zhang, N. A class of catalysts of BiO_X (X = Cl, Br, I) for anchoring polysulfides and accelerating redox reaction in lithium sulfur batteries. *ACS Nano* **2019**, *13*, 13109–13115.

47.　Li, R.; Peng, H.; Wu, Q.; Zhou, X.; He, J.; Shen, H.; Yang, M.; Li, C. Sandwich-like Catalyst–Carbon–Catalyst Trilayer Structure as a Compact 2D Host for Highly Stable Lithium–Sulfur Batteries. *Angew. Chem. Int. Ed. Engl.* **2020**, *59*, 12129–12138.

48.　Wu, F.; Qian, J.; Chen, R.; Zhao, T.; Xu, R.; Ye, Y.; Li, W.; Li, L.; Lu, J.; Amine, K. Sulfur cathode based on layered carbon matrix for high-performance Li–S batteries. *Nano Energy* **2015**, *12*, 742–749.

49.　Jiang, Y.; Liu, H.; Tan, X.; Guo, L.; Zhang, J.; Liu, S.; Guo, Y.; Zhang, J.; Wang, H.; Chu, W. Monoclinic ZIF-8 nanosheet-derived 2D carbon nanosheets as sulfur immobilizer for high-performance lithium sulfur batteries. *ACS Appl. Mater. Interfaces* **2017**, *9*, 25239–25249.

50.　Su, D.; Cortie, M.; Fan, H.; Wang, G. Prussian blue nanocubes with an open framework structure coated with PEDOT as high-capacity cathodes for lithium-sulfur batteries. *Adv. Mater.* **2017**, *29*, 1700587.

51.　Xu, J.; Zhang, W.; Chen, Y.; Fan, H.; Su, D.; Wang, G. MOF-derived porous $N–Co_3O_4@N–C$ nanododecahedra wrapped with reduced graphene oxide as a high capacity cathode for lithium–sulfur batteries. *J. Mater. Chem. A* **2018**, *6*, 2797–2807.